GEOPHYSICS, VOL. 86, NO. 1 (JANUARY-FEBRUARY 2021); P. T45–T59, 21 FIGS.
10.1190/GEO2020-0092.1

Mimetic finite-difference coupled-domain solver for anisotropic media

Harpreet Sethi[1], Jeffrey Shragge[1], and Ilya Tsvankin[1]

ABSTRACT

Accurately modeling full-wavefield solutions at and near the seafloor is challenging for conventional single-domain elastic finite-difference (FD) methods. Because they treat the fluid layer as a solid with zero shear-wave velocity, the energy partitioning for body and surface waves at the seafloor is distorted. This results in incorrect fluid/solid boundary conditions, which has significant implications for imaging and inversion applications that use amplitude information for model building. To address these issues, here we use mimetic FD (MFD) operators to develop and test a numerical approach for accurately implementing the boundary conditions at a fluid/solid interface. Instead of employing a single "global" model domain, we partition the full grid into two subdomains that represent the acoustic and elastic (possibly anisotropic) media. A novel split-node approach based on one-sided MFD operators is introduced to distribute grid points at the fluid/solid interface and satisfy the wave equation and the boundary conditions. Numerical examples demonstrate that such MFD operators achieve stable implementation of the boundary conditions with the same (fourth) order of spatial accuracy as that inside the split-domain interiors. We compare the wavefields produced by the MFD scheme with those from a more computationally expensive spectral-element method to validate our algorithm. The modeling results help analyze the events associated with the fluid/solid (seafloor) interface and provide valuable insights into the horizontal displacement or velocity components (e.g., recorded in ocean-bottom-node data sets). The developed MFD approach can be efficiently used in elastic anisotropic imaging and inversion applications involving ocean-bottom seismic data.

INTRODUCTION

Modeling the full wavefield at or near a fluid/solid interface (i.e., the seafloor) is of significant interest for numerous marine seismic imaging and inversion applications. Correctly implementing the boundary conditions near a fluid/solid interface helps accurately simulate complex wavefield phenomena including energy partitioning of body waves, the generation of Scholte (Stoneley) waves (de Hoop and Van der Hijden, 1984), and leaky Rayleigh modes (Padilla et al., 1999). Modeling seafloor scattering (Robertsson and Levander, 1995) makes it possible to conduct a more complete analysis of four-component (4C) ocean-bottom data (i.e., three-component sensors recording particle velocity and a hydrophone recording pressure; Farfour and Yoon, 2016). A further benefit may be in obtaining more accurate estimates of the shear-wave velocity and anisotropy parameters in marine sediments (Kugler et al., 2007; Tomar et al., 2016).

The correct boundary conditions at a fluid/solid interface involve the continuity of traction (dynamic boundary conditions) and of the vertical velocity or displacement (kinematic boundary condition) (Sun et al., 2017). However, the kinematic boundary conditions are not properly implemented in most conventional finite-difference (FD) algorithms that use an elastic wave-equation solver throughout a single "global" modeling domain and set the S-wave velocity to zero in the fluid (Virieux, 1986; Levander, 1988). This approach assumes the fluid/solid interface to be "welded," which incorrectly implies the continuity of the horizontal displacement or particle velocity at the fluid/solid interface. Such erroneous boundary conditions cause wavefield distortions in simulated surface waves, especially in their horizontal components near the seafloor (De Basabe and Sen, 2014).

The global-domain modeling approach also incurs additional overheads of computing and storing multicomponent elastic wavefields in the acoustic layer. Specifically, the number of the partial wavefield derivatives per grid point required for computation and associated

Manuscript received by the Editor 14 February 2020; revised manuscript received 19 August 2020; published ahead of production 13 October 2020; published online 08 January 2021.
[1]Colorado School of Mines, Golden, Colorado 80401-1887, USA. E-mail: hsethi@mymail.mines.edu (corresponding author); jshragge@gmail.com; ilya@mines.edu.

DOI:10.1190/geo2020-0092.1

storage when using an elastic FD solver is approximately two (in 2D) or three (in 3D) times that of an acoustic solver. An alternative strategy is to use a partitioned-grid approach (Komatitsch et al., 2000; Käser and Dumbser, 2008; Sun et al., 2017) where one solves the acoustic wave equation in the fluid and the elastic wave equation in the solid on separate grids. The solutions in these two domains are coupled at each time step via the explicit boundary conditions. This approach has been developed for flat and curved fluid/solid interfaces using different numerical methods.

For example, Stephen (1983) uses a conventional FD approach for a flat seafloor to study different types of surface waves. His algorithm assumes constant elastic parameters near the interface and introduces an imaginary elastic boundary in the fluid. Hung and Forsyth (1998) study wave propagation in inhomogeneous anisotropic media using high-order Chebyshev and Fourier differential pseudospectral operators. Komatitsch et al. (2000) develop a spectral-element method (SEM) that handles flat and curved interfaces and achieves a high-order [i.e., greater than $O(\Delta x^4)$, where $O(\Delta x^4)$ denotes fourth-order spatial accuracy] accurate solution. However, this numerical scheme is computationally expensive and the procedure for creating a satisfactory non-flat 3D mesh conforming to the physical boundaries is complicated (de la Puente et al., 2014). Other approaches for incorporating a fluid/solid interface include the discontinuous Galerkin (Kaser and Dumbser, 2008) and finite-volume (Voinovich et al., 2003) methods. However, the algorithmic complexity and computational/memory costs of these techniques prevent their application in industry-scale 3D anisotropic elastic wavefield modeling, imaging, and inversion.

FD methods are often used for modeling seismic wavefields in a fluid/solid configuration because of their well-developed and easy-to-implement numerical schemes, compact FD stencils that port well to GPU architectures, and a moderate computational cost. However, FD implementations experience difficulties for curved or irregular interfaces where a Cartesian model discretization gives rise to unphysical staircase diffractions (Muir et al., 1992). FD methods have been applied on curvilinear grids conformal to free-surface topography, which reduces these numerical errors and streamlines implementation of the boundary conditions (Zhang et al., 2012; Shragge, 2014; Petersson and Sjögreen, 2015). For example, Sun et al. (2017) present a curvilinear-coordinate FD approach to handle a fluid/solid split-domain configuration using collocated-grid MacCormack-based FD stencils. Also, they use one-sided FD operators to implement the boundary conditions. However, the spatial accuracy of this scheme reduces to $O(\Delta x^2)$ near the interface, as opposed to $O(\Delta x^4)$ within the domain interior. Hence, it is necessary to apply wavefield smoothing near the interface to mitigate numerical instability. These issues are indicative of the typical challenges for FD-based methods in achieving uniform numerical accuracy because such instabilities arise at all domain boundaries and interfaces with strong contrasts in material properties.

Recently introduced mimetic FD (MFD) operators (Castillo and Miranda, 2013) preserve the underlying physics of the employed partial differential equations (PDEs) in the discretization process. De la Puente et al. (2014) present an MFD approach for solving the elastic wave equation for models with topography using a fully-staggered-grid (FSG) scheme (Lebedev, 1964; Lisitsa and Vishnevskiy, 2010). Shragge and Tapley (2017) and Shragge (2017) use a tensorial formulation of the acoustic and elastic wave equations discretized with MFD operators to model wavefields on deformed grids and implement flux-preserving boundary conditions. Qu et al. (2020) present an MFD approach for acoustic/elastic coupling at the seafloor based on a curvilinear coordinate mesh. Konuk and Shragge (2020) directly incorporate a time-varying sea surface into the space-time geometry of the acoustic wave equation and solve that equation using an MFD/FSG approach.

Here, we develop and test a novel partitioned-grid approach to extend the MFD solutions to models with a fluid/solid interface. Our algorithm generates stable wavefield solutions that honor the correct fluid/solid boundary conditions and have the same order of numerical accuracy in the acoustic and elastic domains. First, we briefly discuss the relevant elements of wave-propagation theory in acoustic and elastic media and describe the boundary conditions for a fluid/solid interface. Then, we introduce the MFD method and its implementation for a fluid/solid boundary using a split-node approach. Numerical examples for 2D models with fluid/fluid and fluid/solid interfaces illustrate the accuracy of the developed solution. In particular, the method is shown to be applicable to seafloor models that include underwater transversely isotropic layers with a vertical symmetry axis (VTI). Finally, we discuss the advantages and limitations of the proposed MFD algorithm.

THEORY

The 3D elastic wave equation in a heterogeneous anisotropic medium can be written as

$$\rho^s \dot{v}_i^s = \partial_j \sigma_{ij} + b_i, \tag{1}$$

where ρ^s is the density, v_i^s is the ith component of the particle velocity, the dot marks the temporal derivative, σ_{ij} is the stress tensor, ∂_j denotes differentiation with respect to the spatial coordinates, b_i is the body force per unit volume, and the superscript s indicates a material property or wavefield variable defined in the solid domain. We also use the following linear constitutive relationship (generalized Hooke's law) to link the temporal derivatives of the stress (σ_{ij}) and strain (ϵ_{kl}) tensors,

$$\dot{\sigma}_{ij} = C_{ijkl}\,\dot{\epsilon}_{kl}, \tag{2}$$

where C_{ijkl} is the stiffness tensor, and

$$\dot{\epsilon}_{kl} = \frac{1}{2}\left(\partial_l v_k^s + \partial_k v_l^s\right). \tag{3}$$

In fluid regions, the wavefield is described by coupled PDEs that represent the conservation of linear momentum,

$$\rho^f \dot{v}_i^f + \partial_i p = b_i, \tag{4}$$

and the conservation of mass,

$$\dot{p} + \rho^f (c^f)^2 \partial_i v_i^f = 0, \tag{5}$$

where ρ^f is the fluid density, p is the pressure, v_i^f is the particle velocity, and c^f is the velocity of acoustic waves; the superscript "f" indicates a material property or wavefield variable defined in the fluid.

Fluid/solid boundary conditions

The boundary conditions coupling the elastic (possibly anisotropic) and acoustic layers are the continuity of traction and of the normal

component of the particle velocity. The normal ($\hat{n}$) to a flat interface located at $z = z_0$ is oriented vertically ($\hat{n} = \hat{z}$), so the continuity of traction (i.e., the "dynamic" boundary condition) is given by

$$(\sigma_{zz} + p)|_{z=z_0} = 0, \tag{6}$$

whereas

$$\sigma_{zx}|_{z=z_0} = 0, \tag{7}$$

because an inviscid fluid does not support shear stress. The continuity of the normal (vertical) component of the particle velocity (i.e., the kinematic boundary condition) is expressed as

$$(v_z^f - v_z^s)|_{z=z_0} = 0. \tag{8}$$

Figure 1 illustrates the fluid and solid regions coupled at a horizontal interface $z = z_0$. To satisfy the boundary conditions in equations 6–8, it is convenient to define the acoustic and elastic material properties on the same nodes at the interface. This allows for physical collocation of the interface nodes with the fluid/solid interface, which facilitates higher-order implementations of the boundary conditions, as discussed below.

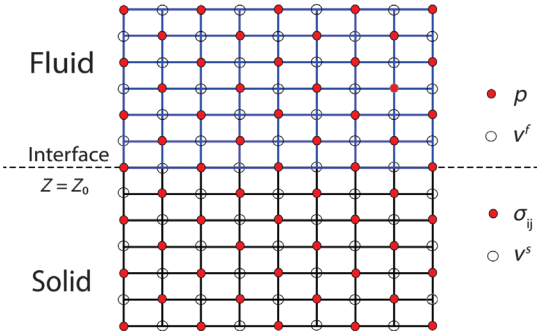

Figure 1. 2D nodal distribution near a fluid/solid interface. Blue and black colors mark the fluid and solid regions, respectively. Open circles in the fluid and solid correspond to v_i^f and v_i^s, respectively, and red points in the fluid and solid correspond to p and σ_{ij}, respectively. All variables are defined at the interface located at $z = z_0$.

Mimetic finite differences and fully staggered grids

Generating high-order [i.e., $O(\Delta x^4)$ or greater] accurate implementations of the fluid/solid boundary conditions specified in equations 6–8 remains a challenge for standard FD methods. As mentioned above, existing FD solutions that simultaneously satisfy the acoustic and elastic (anisotropic) wave equations and the boundary conditions have numerical accuracy of $O(\Delta x^2)$ or lower and tend to become unstable. In addition, many FD boundary-condition implementations introduce unphysical ghost points to ensure the continuity of the wavefield derivatives obtained with two-sided FD operators (Sun et al., 2017). Also, the wave-equation discretization using standard Taylor-series-based FD operators does not honor such underlying physical concepts as the flux conservation laws and tensorial calculus properties that are naturally satisfied by their continuum counterparts (Castillo and Grone, 2003). These shortcomings lead to numerical instability and errors in the simulated wavefields.

We address these issues by using MFD operators (Castillo and Grone, 2003; Rojas, 2007; Corbino and Castillo, 2017). The mimetic divergence and gradient FD operators (**D** and **G**) honor global conservation laws (Castillo and Grone, 2003) and can be constructed with high-order accuracy [i.e., $O(\Delta x^4)$ or greater] throughout the whole computational domain including the boundaries and partitioned interfaces (Castillo and Miranda, 2013; Corbino and Castillo, 2017). These properties make one-sided MFD operators suitable for implementing the boundary conditions with higher-order accuracy.

To illustrate the difference between 1D MFD operators and their standard 1D FD counterparts, Figure 2a–2c displays the operators **D**, **G**, and the standard Taylor-series-based FD operators, respectively, which have the same $[O(\Delta x^4)]$ order of accuracy for an $N = 8$ point domain. Appendix A presents the FD coefficients (marked by different colors in Figure 2), as well as the dimensions of **D**, **G**, and the standard Taylor-based operators. Note that the interior rows of the three operators are the same in all three panels; therefore, the MFD operators converge toward their Taylor-based FD counterparts within the domain interior. The only differences

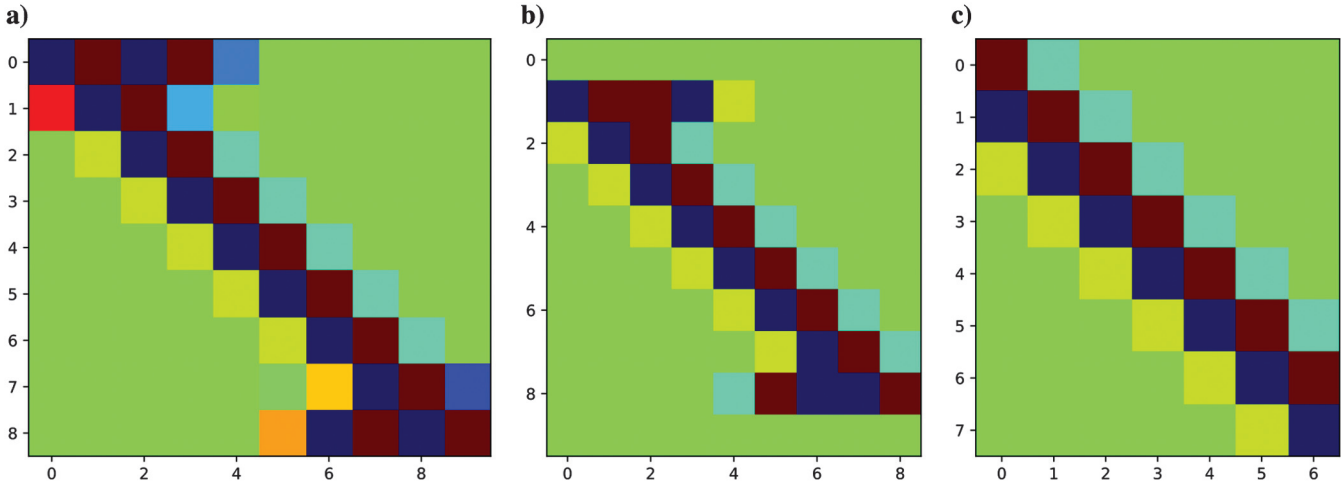

Figure 2. 1D mimetic and Taylor-series-based FD operators that have the $O(\Delta x^4)$ accuracy for $N = 8$. (a) The mimetic gradient $\mathbf{G} \in \mathbb{R}^{(9,10)}$, (b) the mimetic divergence $\mathbf{D} \in \mathbb{R}^{(10,9)}$, and (c) the Taylor-series-based FD derivative operator.

DOI:10.1190/geo2020-0092.1

are near the boundary where the MFD operators include additional terms to ensure flux conservation (Castillo and Miranda, 2013; Corbino and Castillo, 2017).

We use a FSG approach to implement the MFD scheme because such grid layout increases the numerical stability of the computed wavefields by making all wavefield partial derivatives available at all grid points (de la Puente et al., 2014; Shragge and Tapley, 2017). In contrast to standard staggered grids (SSGs), no costly high-order interpolation of the partial derivatives is required (Lisitsa and Vishnevskiy, 2010; de la Puente et al., 2014). Using an FSG system is particularly beneficial for lower-symmetry anisotropic models including the most general, triclinic symmetry (Lisitsa and Vishnevskiy, 2010).

For simplicity we first discuss the 1D MFD FSG implementation. Then the solutions are extended to 2D models that include the free surface and a fluid/solid interface. To distinguish the variables representing continuous wavefield and material properties in equations 1–8 from their discrete counterparts, we use bold symbols to denote discrete gradient and divergence operators and bars for discrete wavefield and material property variables.

1D MFD FSG implementation

An FSG system consists of multiple intertwined grids like those in an SSG; however, their implementation depends on the dimensionality of the grids. A 1D FSG system is equivalent to the system used in a 1D SSG approach. We use two staggered field grids, $\mathbf{f} \in \mathbb{R}^{N+2}$ and $\mathbf{v} \in \mathbb{R}^{N+1}$, where $\mathbf{f}$ is defined at the cell centers and $\mathbf{v}$ at the grid nodes (i.e., cell boundaries). Figure 3a shows an example of 1D MFD FSG for an $N = 8$ point model domain. In the fluid domain, $\mathbf{f}$ and $\mathbf{v}$ represent the pressure $\bar{p}$ and particle velocity $\bar{v}_i^f$, respectively, whereas in the solid domain, $\mathbf{f}$ and $\mathbf{v}$ represent the stress $\bar{\sigma}_{ij}$ and particle velocity $\bar{v}_i^s$, respectively.

Because an MFD solution requires all variables to be also defined at the domain boundaries (i.e., interfaces), the corresponding variables represented by $\mathbf{f}$ and $\mathbf{v}$ grids share the same spatial locations. In Figure 3a these extra locations are referred to as *mimetic points*, which are required for higher-order implementation of the derivative operators near the boundaries. The mimetic gradient matrix operator $\mathbf{G}$ acts on the field variables defined on the $\mathbf{f}$-grid at the cell centers and maps them to form the vector defined on the $\mathbf{v}$-grid at the cell boundaries. Similarly, the mimetic divergence matrix operator $\mathbf{D}$ acts on the field variables defined on the $\mathbf{v}$-grid at the cell boundaries and maps them to cell centers to form the vector defined on the $\mathbf{f}$-grid. For the 1D elastic wave equations 1–3 we update the $\dot{\bar{v}}_z^s$-field in the solid region on the $\mathbf{v}$-grid according to

$$\dot{\bar{v}}_z^s = (\bar{\rho}^s)^{-1} G\, \bar{\sigma}_{zz} + \bar{b}_z, \tag{9}$$

and the field $\dot{\bar{\sigma}}_{zz}$ on the f-grid using

$$\dot{\bar{\sigma}}_{zz} = \bar{C} D\, \bar{v}_z^s, \tag{10}$$

where $\bar{C}$ is an arbitrarily anisotropic stiffness matrix. Similarly, for the acoustic wave equation we update fluid particle velocity $\dot{\bar{v}}_z^f$ on the $\mathbf{v}$-grid via

$$\dot{\bar{v}}_z^f = -(\bar{\rho}^f)^{-1} G \bar{p}, \tag{11}$$

and the pressure field $\dot{\bar{p}}$ defined on f through

$$\dot{\bar{p}} = -\bar{\rho}^f (\bar{c})^2 D\, \bar{v}_z^f. \tag{12}$$

It is important to note that the MFD operators applied to the boundary region include the contribution of the extra f_M mimetic points. For example, the gradient can be expressed numerically at the left boundary $z_{M_1} = -4\Delta z$ where $M_1 = -4$ in Figure 3a as

$$\left.\frac{\partial f}{\partial z}\right|_{z=-4\Delta z} \asymp G_{(0,0)}\, f_{M_1} + \sum_{l=1}^{P_G} G_{(0,l)}\, f_{l+M_1-1/2}. \tag{13}$$

Likewise, for the right boundary point at $z_{M_2} = 4\Delta z$ where $M_2 = 4$,

$$\left.\frac{\partial f}{\partial z}\right|_{z=4\Delta z} = G_{(N+1,N+2)} f_{M_2} + \sum_{l=N-P_G}^{N} G_{(N+1,l)} f_{l-M_2-1/2}, \tag{14}$$

where P_G is the bandwidth (i.e., the number of nonzero coefficients) of the mimetic gradient operator, N is the domain size, f_{M_1} and f_{M_2} are the mimetic points on the left and right boundary at locations $z_{(M_1=-4)}$ and $z_{(M_2=4)}$, respectively, and $G_{(0,l)}$ and $G_{(N+1,l)}$ are the first and last rows of the gradient operator, respectively. The derivatives in equations 13 and 14 contribute to just one row of the matrix operator vectors $G\,\bar{\sigma}_{zz}$ and $G\bar{p}$ in equations 9 and 11.

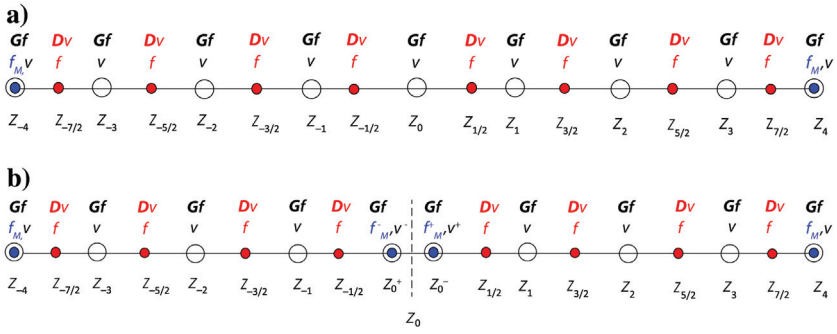

Figure 3. (a) Example of a 1D MFD FSG for $N = 8$. (b) Example of a 1D MFD-FSG with split nodes for $N = 8$ with an interface at $z = z_0$. Red points denote $\mathbf{f} \in \{\bar{p}, \bar{\sigma}_{ii}\}$, open circles denote $\mathbf{v} \in \{\bar{v}_i^f, \bar{v}_i^s\}$ and f_M (in blue) denotes mimetic points.

2D MFD FSG implementation

In the 2D MFD implementation, an FSG is equivalent to two complementary coupled grid systems (i.e., two SSGs) that are staggered in the horizontal and vertical directions by $\Delta x/2$ and $\Delta z/2$. Figure 4a shows a system of two coupled SSGs where we use the grids $[\mathbf{f}, \mathbf{f}] \in \mathbb{R}^{(N+2)\times(N+2)}$ and $[\mathbf{v}, \mathbf{v}] \in \mathbb{R}^{(N+1)\times(N+1)}$ to represent $\bar{p}$ and $\bar{\sigma}_{ij}$ for the acoustic and elastic media, respectively. Similarly, Figure 4b shows the complementary system of two coupled SSGs where the grids $[\mathbf{f}, \mathbf{v}] \in \mathbb{R}^{(N+2)\times(N+1)}$ and $[\mathbf{v}, \mathbf{f}] \in \mathbb{R}^{(N+1)\times(N+2)}$ represent $\bar{v}_i^f$ and $\bar{v}_i^s$ for the acoustic and elastic media, respectively. Note that the wavefields are explicitly defined in this manner because other definitions lead to spurious wavefield solutions (Lisitsa and Vishnevskiy, 2010), especially for TTI (transversely isotropic with a tilted symmetry axis) media. The extension

to 3D models is straightforward, but involves intertwining four SSGs to form a single FSG cell.

Figure 5 shows a single-cell FSG nodal distribution near a domain boundary denoted by $z = z_{-M}$, where all field variables (i.e., $\bar{v}_i^s$ or $\bar{\sigma}_{ij}^s$) share a common location. In a single cell comprising the FSG, the four corner points of the $[\mathbf{v},\mathbf{v}]$-grid (hollow circles at the corners of the FSG cell in Figure 4a) and one corner of the complementary $[\mathbf{f},\mathbf{f}]$-grid (hollow circle at the center of the cell in Figure 4a) contribute to updating the variables $\bar{p}$ and $\bar{\sigma}_{ij}$. Likewise, the top left and right corners of the $[\mathbf{v},\mathbf{f}]$-grid (left and right edge centers in the FSG cell in Figure 4b) and top and bottom left corners of the complementary $[\mathbf{f},\mathbf{v}]$-grid (top and bottom edge centers in the FSG cell in Figure 4b) contribute to updating the variables $\bar{v}_i^s$ and $\bar{v}_i^f$.

The mimetic gradient and divergence operators in 2D MFD FSG act in the z- and x-directions (e.g., $G_{\mathbf{z}}$ and $G_{\mathbf{x}}$, $D_{\mathbf{z}}$ and $D_{\mathbf{x}}$) in the same cyclic fashion as in 1D implementations (Shragge and Tapley, 2017). The only difference is in the computation of the partial derivatives near the domain boundaries where there are two types of boundary nodes, $N1$ and $N2$, which differ in terms of the extra mimetic points. An $N2$-type node includes extra pressure ($\bar{p}_M$) and stress ($\bar{\sigma}_{ij_M}$) mimetic points defined on the $[\mathbf{f},\mathbf{f}]$-grids in the acoustic and elastic regions, respectively. An $N1$-type node includes the extra velocity ($\bar{v}_M^f$ and $\bar{v}_M^s$) mimetic points defined on the $[\mathbf{f},\mathbf{v}]$- and $[\mathbf{v},\mathbf{f}]$-grids in the same regions. For the nodes along the $\mathbf{f}$- and $\mathbf{v}$-grids one needs to use the following FD stencils to compute the derivatives:

$$\left.\frac{\partial f}{\partial z}\right|_{k_1} G_{(k_1,0)}\, f_M + \sum_{l=1}^{P_G} G_{(k_1,l)}\; f_{l+1/2}, \tag{15}$$

and

$$\left.\frac{\partial v}{\partial z}\right|_{k_1+1/2} \approx \sum_{l=0}^{P_D} D_{(k_1,l)}\, v_l, \tag{16}$$

where k_1 is the depth location on the grid, $\mathbf{f}$ and $\mathbf{v}$ represent $\bar{p}$ and $\bar{\sigma}_{ij}$ for $N1$-type nodes and $\bar{v}_i^f$ and $\bar{v}_i^s$ for $N2$-type nodes, and P_G and P_D represent the bandwidth of the mimetic gradient and mimetic divergence operators, respectively.

Implementation for 1D fluid/solid interface

We implement the algorithm for a fluid/solid boundary using the MFD operators and the split-node approach described above (Rojas et al., 2008), where the full domain is partitioned by the interface into two computational subdomains. Figure 3b displays a 1D MFD FSG split-node grid again for $N = 8$ points. The node z_0 is partitioned at the interface into the nodes z_0^- and z_0^+ that are physically collocated but defined in the different subdomains.

We represent the discrete $\mathbf{v}$- and $\mathbf{f}$-grid components in terms of the values of $\mathbf{v}$ at the cell nodes and $\mathbf{f}$ at the cell centers using the split-node approach:

$$\mathbf{v} = \begin{bmatrix} v^- \\ v^+ \end{bmatrix} \quad \text{and} \quad \mathbf{f} = \begin{bmatrix} f^- \\ f^+ \end{bmatrix}, \tag{17}$$

where for $N = 8$ points,

$$v^- = [v(z_{-4}), v(z_{-3}), v(z_{-2}), v(z_{-1}), v(z_{0^-})], \tag{18}$$

$$v^+ = [v(z_{0^+}), v(z_1), v(z_2), v(z_3), v(z_4)], \tag{19}$$

and

$$f^- = [f(z_{-4}), f(z_{-\frac{7}{2}}), f(z_{-\frac{5}{2}}), f(z_{-\frac{3}{2}}), f(z_{-\frac{1}{2}}), v(z_{0^-})], \tag{20}$$

$$f^+ = [f(z_{0^+}), f(z_{\frac{1}{2}}), f(z_{\frac{3}{2}}), f(z_{\frac{5}{2}}), f(z_{\frac{7}{2}}), f(z_4)]. \tag{21}$$

We construct augmented mimetic divergence and gradient matrix operators, D_z^A and G_z^A, which are applied separately on both sides of the interface:

$$D_z^A = \begin{bmatrix} D_{z_-}^{(4)} & 0 \\ 0 & D_{z_+}^{(4)} \end{bmatrix}, \tag{22}$$

and

$$G_z^A = \begin{bmatrix} G_{z_-}^{(4)} & 0 \\ 0 & G_{z_+}^{(4)} \end{bmatrix}, \tag{23}$$

where $D_{z_-}^{(4)} = D_{z_+}^{(4)} = D_z^{(4)}$ (i.e., the standard 1D mimetic divergence operator) and $G_{z_-}^{(4)} = G_{z_+}^{(4)} = G_z^{(4)}$ (i.e., the standard 1D mim-

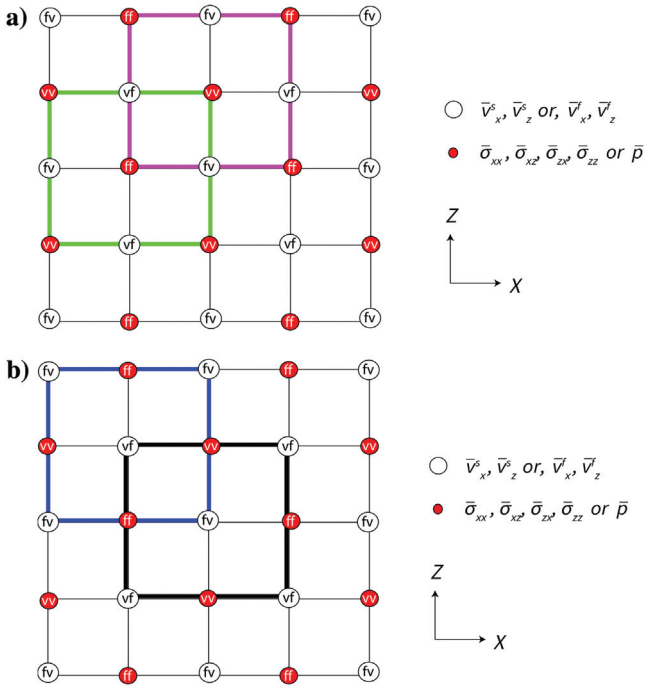

Figure 4. Coupled system of SSGs inside a 2D MFD FSG. (a) The $[\mathbf{f},\mathbf{f}]$- and $[\mathbf{v},\mathbf{v}]$-grids in magenta and green colors, respectively. The four red points (either $\bar{p}$ or $\bar{\sigma}_{ij}$) form the corners of both grids. (b) The $[\mathbf{f},\mathbf{v}]$- and $[\mathbf{v},\mathbf{f}]$-grids in blue and black color, respectively. The four hollow circles (either $\bar{v}_i^s$ or $\bar{v}_i^f$) form the corners of both grids.

etic gradient operator). The submatrix $D^{(4)}_{z^-}$ acts on v^- at the cell nodes to map the v^- values to f^- (excluding z_{-4} and z_{0^-}) at the cell centers, whereas $D^{(4)}_{z^+}$ acts on v^+ at the cell nodes and maps them to f^+ (excluding z_4 and z_{0^+}). Similarly, the submatrix $G^{(4)}_{z^-}$ acts on f^- at the cell centers to map them to v^- at the cell nodes, whereas $G^{(4)}_{z^+}$ acts on f^+ at the cell centers to map them to v^+ at the cell nodes.

Figure 6 illustrates the augmented $O(\Delta x^4)$ mimetic gradient operator for $N^+ = N^- = 10$, where N^+ and N^- are the domain sizes on both sides of the interface. The interface node is located at the intersection of the vertical and horizontal lines. It is important to note that the interior coefficients of mimetic operators again are exactly the same as those of Taylor-series-based FD operators. However, the coefficients near the interfaces are different as a result of satisfying the flux conservation laws and higher-order spatial accuracy requirements in MFD implementations.

The boundary conditions for the field variables defined on the **v**-grids are implemented using an averaging scheme. In the 1D acoustic/elastic case, the **v**-grid corresponds to $\bar{v}^s_z$ and $\bar{v}^f_z$, so both quantities are replaced by $(\bar{v}^s_z + \bar{v}^f_z)/2$ at the interface. For the variables defined on the **f**-grids, we use the continuity of the normal-velocity component to update the mimetic pressure and stress. Equation 8 implies that

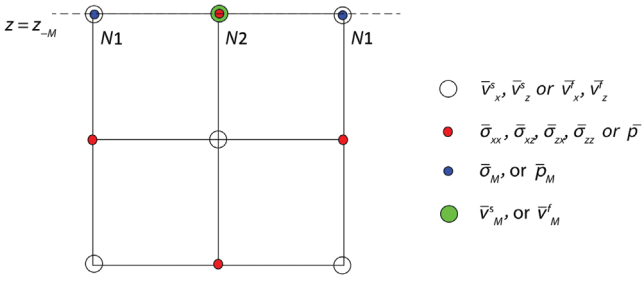

Figure 5. 2D MFD FSG nodal distribution in a single cell near a boundary at $z = z_{-M}$. Red points denote the stress $\bar{\sigma}^s_{ij}$ (solid) and pressure $\bar{p}^f$ (fluid). Hollow circles denote $\bar{v}^s_i$ (solid) and $\bar{v}^f_i$ (fluid). Blue and green points mark the additional mimetic points at the domain boundary.

$$\dot{\bar{v}}^f_z|_{z=z_0^-} = \dot{\bar{v}}^s_z|_{z=z_0^+}. \tag{24}$$

Using equations 9, 11, and 13 (assuming $\bar{f}_z = 0$), we obtain the following boundary condition:

$$\bar{\rho}_f^{-1}\Big(G_{z(M+1,M+2)}\bar{p}_M + \sum_{l=M-P_G}^{M} G_{z(M+1,l)}\bar{p}^{l+1/2}\Big) = -\bar{\rho}_s^{-1}\Big(G_{z(0,0)}\bar{\sigma}_M + \sum_{l=1}^{P_G} G_{z(0,l)}\bar{\sigma}^{l+1/2}_{zz}\Big). \tag{25}$$

Because $\bar{\sigma}_M = -\bar{p}_M$ at the interface (equation 6), we may rewrite equation 25 as

$$\bar{\sigma}_M = \frac{-\bar{\rho}_s \sum_{l=M-P_G}^{M} G_{z(M+1,l)}\bar{p}^{l+1/2} - \rho_f \sum_{l=1}^{P_G} G_{z(0,l)}\bar{\sigma}^{l+1/2}_{zz}}{G_{z(M+1,M+2)}\bar{\rho}_s - G_{z(0,0)}\bar{\rho}_f}, \tag{26}$$

where $\bar{p}^{l+1/2}$ and $\bar{\sigma}^{l+1/2}_{zz}$ are defined at the cell centers, $\bar{p}_M$ is the mimetic pressure at the interface node z_0^-, and $\bar{\sigma}_M$ is the mimetic stress at the interface node z_0^+.

Coupling 2D FSGs at fluid/solid interface

For 2D models, there are two complementary coupled grid systems comprised of four total grids (see Figure 4a and 4b). Similar to the 1D case, we apply an averaging scheme to the $[\mathbf{v},\mathbf{v}]$- and $[\mathbf{v},\mathbf{f}]$-grids to implement the boundary conditions. We replace $\bar{v}^s_z$ and $\bar{v}^f_z$ defined on the $[\mathbf{v},\mathbf{v}]$-grids by $(\bar{v}^s_z + \bar{v}^f_z)/2$, and substitute $\bar{\sigma}_{zz}$ and $\bar{p}$ defined on the $[\mathbf{v},\mathbf{f}]$-grids with $(\bar{\sigma}_{zz} - \bar{p})/2$ and $(-\bar{\sigma}_{zz} + \bar{p})/2$, respectively.

Figure 7 illustrates the nodal distribution for the 2D MFD FSG near the boundary by showing the two node types ($N1$ and $N2$) that contribute to the wavefield derivatives at the interface. The mimetic points can be updated in a fashion similar to that in 1D applications. Using the temporal derivatives of the boundary conditions (equations 6 and 8) and the discrete form of the wave equation makes it possible to solve for the mimetic points corresponding to $\bar{\sigma}_{zz}$, $\bar{p}$, $\bar{v}_x$, and $\bar{v}_z$ following the approach presented in equations 24–26.

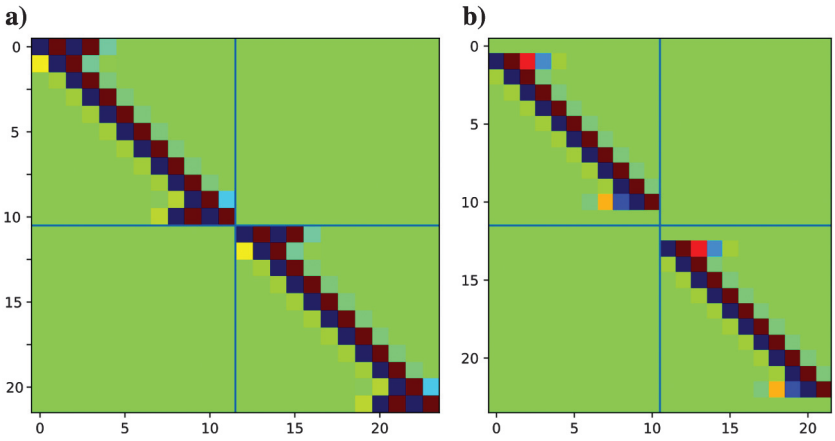

Figure 6. Augmented (a) gradient $\mathbf{G}^{\mathbf{A}}_{\mathbf{z}}$ and (b) divergence $\mathbf{D}^{\mathbf{A}}_{\mathbf{z}}$ MFD operators that have the $O(\Delta x^4)$ order of accuracy for $M + N = 20$.

Source injection and wavefield extraction

The coupling of multiple grids in FSG requires distributed source injection and wavefield extraction. For central cell injection and extraction (Figure 4a), the $\bar{\sigma}^s_{ij}$ and $\bar{p}$ wavefields defined on the $[\mathbf{f},\mathbf{f}]$- and $[\mathbf{v},\mathbf{v}]$-grids contribute five points in an FSG cell. For source injection, the source at any $[\mathbf{f},\mathbf{f}]$-grid point is injected with the weight equal to unity and four $[\mathbf{v},\mathbf{v}]$ grid points are injected with a weight of 1/2. However, for wavefield extraction the weights are 1/2 for the $[\mathbf{f},\mathbf{f}]$-grid point and 1/4 for four $[\mathbf{v},\mathbf{v}]$-grid points (Lisitsa and Vishnevskiy, 2010). The wavefields $\bar{v}^s_i$ and $\bar{v}^f_i$ defined on the $[\mathbf{f},\mathbf{v}]$- and $[\mathbf{v},\mathbf{f}]$-grids contribute four points in the same FSG cell (Figure 4b). For source in-

DOI:10.1190/geo2020-0092.1

jection we use a weight of 1/2 for the $[\mathbf{f},\mathbf{v}]$- and $[\mathbf{v},\mathbf{f}]$-grid points, whereas for wavefield extraction the weight is 1/4 for the $[\mathbf{f},\mathbf{v}]$- and $[\mathbf{v},\mathbf{f}]$-grid points.

Free-surface implementation

The mimetic nodes at the free surface can be updated in a fashion similar to the fluid/solid interface implementation described above. Because in the fluid/solid scenario the model always has an acoustic free surface, the equation for updating mimetic points follows from the zero-pressure condition at that surface. The velocities at the free-surface mimetic points can be updated as

$$\bar{v}_z^M = \frac{1}{G_z(0,0)}\left(-\sum_{j=0}^{N_G} G_x(i,j)\,\bar{v}_x^{l+1/2} - \sum_{j=1}^{N_G} G_z(0,j)\,\bar{v}_z^{l+1/2}\right), \tag{27}$$

and

$$\bar{v}_x^M = \frac{1}{G_z(0,0)}\left(-\sum_{j=0}^{N_G} G_x(i,j)\,\bar{v}_z^{l+1/2} - \sum_{j=1}^{N_G} G_z(0,j)\,\bar{v}_z^{l+1/2}\right). \tag{28}$$

NUMERICAL EXAMPLES

We test the MFD-FSG split-domain modeling algorithm for fluid/fluid and fluid/solid interfaces using the $O(\Delta x^4)$ mimetic gradient and divergence operators. The results are compared with the solutions obtained from the spectral-element method (SEM; Komatitsch et al., 2000). We also compute single-domain (i.e., "welded") solutions to demonstrate the errors caused by incorrect boundary conditions at the fluid/solid interface.

2D fluid/fluid interface

Here, we consider a 2D fluid/fluid model with the same material properties (velocity and density) on both sides of the interface. In this case all energy is supposed to be transmitted across the boundary and the model should behave as a homogeneous fluid medium. The boundary conditions for the fluid/fluid interface at $z = z_0$ are the continuity of pressure,

$$(\bar{p}^- - \bar{p}^+)|_{z=z_0} = 0, \tag{29}$$

and of the particle-velocity component normal to the interface (i.e., $\hat{n} = \hat{z}$),

$$(\bar{v}_z^- - \bar{v}_z^+)|_{z=z_0} = 0. \tag{30}$$

The model is represented by a 400×400 domain with a grid spacing of $\Delta x = \Delta z = 4$ m. We inject a Ricker-wavelet source with the 30-Hz peak frequency at [x,z] = [800,200] m. The interface is located at $z_0 = 800$ m and the receiver line is 4 m below the fluid/fluid interface. We implement a convolutional perfectly matched layer (C-PML) (Komatitsch and Martin, 2007) boundary condition on the three sides of the model and, therefore, expect to record only the direct P-wave and the free-surface reflection.

Figure 8 shows snapshots of the pressure wavefield $\bar{p}$ obtained using the wavefield extraction procedure discussed above. As desired, more than 99.9% of the energy is transmitted across the interface. For a more quantitative comparison, we compare the $\bar{v}_z$- and $\bar{v}_x$-components recorded at three receiver locations with those from the single-domain (i.e., welded) solution. Because an inviscid fluid cannot support shear stress, our coupled and welded solutions should exactly match. Figure 9 shows the $\bar{v}_z$- and $\bar{v}_x$-components

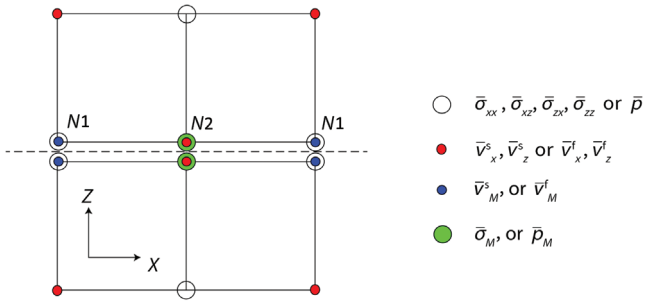

Figure 7. Illustration of a 2D MFD FSG nodal distribution at the interface marked by the dotted line at $z = z_0$. Red points denote $\bar{p}$ and $\bar{\sigma}_{ij}$, hollow circles denote $\bar{v}_i^s$ and $\bar{v}_i^f$, blue circles on the $N1$-type nodes denote $\bar{p}_M$ and $\bar{\sigma}_M$, and green circles on the $N2$-type nodes denote $\bar{v}_M^f$ and $\bar{v}_M^s$ for the fluid (f) and solid (s) media, respectively.

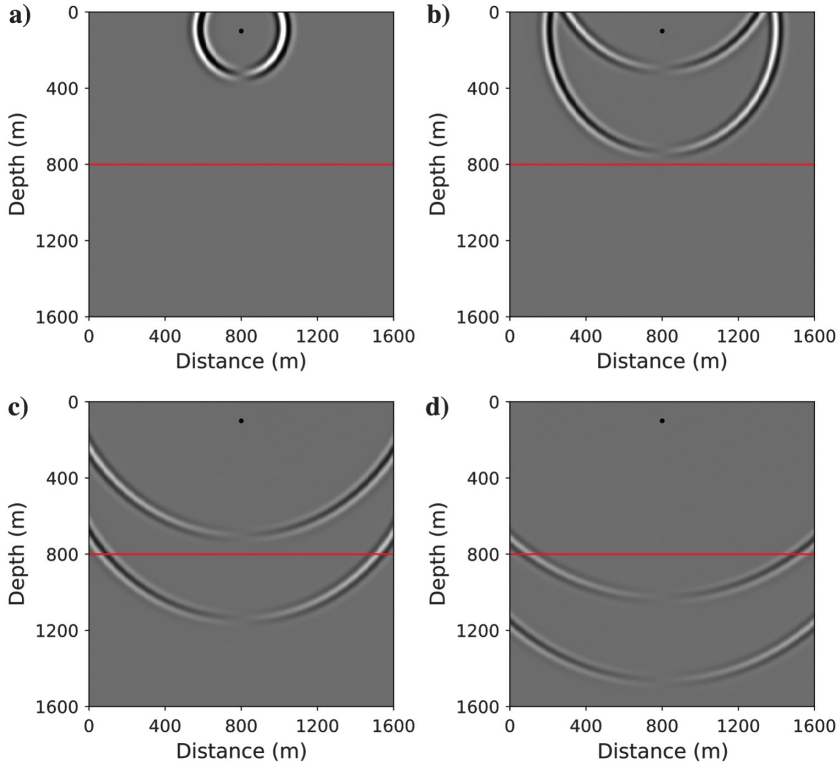

Figure 8. Pressure snapshots at times (a) 0.15 s, (b) 0.30 s, (c) 0.45 s, and (d) 0.57 s. The fluid has velocity $c^f = 2500$ m/s and density $\rho^f = 1000$ kg/m^3. The red line marks the domain boundary at $z = 400$ m. Black dots mark the source locations.

computed from the coupled-domain (cyan), single-domain (yellow), and SEM (magenta) solutions. The good match between all three waveforms confirms the accuracy of our approach and validates our implementation of the boundary conditions.

2D fluid/solid interface

In the next test, the fluid overlays an isotropic solid medium. The model size is 600×220 with a uniform grid spacing of 4 m; the interface is located at $z_0 = 80$ m. We inject a Ricker-wavelet source with the 10 Hz peak frequency at $[x,z] = [1200,64]$ m. The receiver line is located in the solid medium 4 m below the interface ($z = 84$ m). In this experiment we do not expect the coupled-domain and SEM solutions to match the welded one because the latter implements incorrect boundary conditions.

The shot gathers for the coupled-domain $\bar{v}_z$- and $\bar{v}_x$-components are clearly different from those computed by the welded approach (Figure 10). To compare the wavefields produced by the three methods, we analyze both velocity components at the locations marked by the vertical lines at x = 608, 1250, and 1688 m ($z = 104$ m) in Figure 10. Our coupled-domain result (cyan) closely matches the SEM solution (magenta), whereas the welded approach (yellow) produces apparent distortions in the event phases and amplitudes on the $\bar{v}_z$- and $\bar{v}_x$-components (Figure 11).

For further analysis of the wavefield, we applied the coupled-domain solver to the same model with the C-PML conditions on all four sides including the top. Most of the energy on the

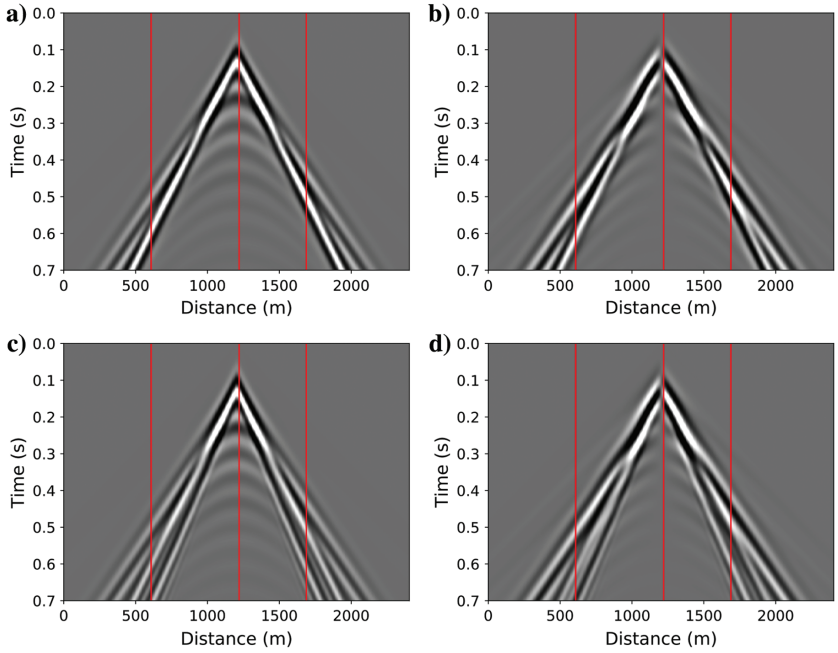

Figure 10. Shot gathers for a 2D fluid/solid model. The solid is isotropic with P-wave velocity $V_P = 2500$ m/s, S-wave velocity $V_S = 1600$ m/s, and density $\rho^s = 2000$ kg/m^3; the fluid has velocity $c^f = 1500$ m/s and density $\rho^f = 1000$ kg/m^3. The coupled-domain solutions for the (a) $\bar{v}_z$- and (b) $\bar{v}_x$-components. The welded-domain solutions for the (c) $\bar{v}_z$- and (d) $\bar{v}_x$-components.

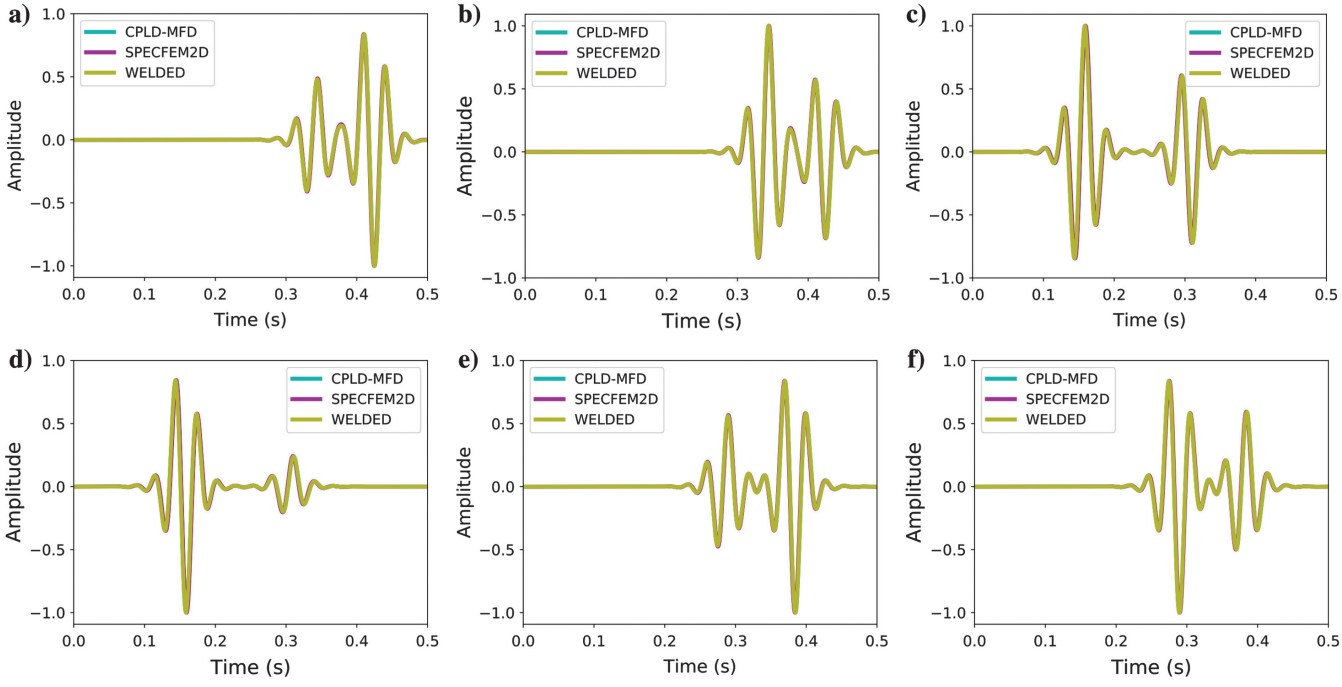

Figure 9. Normalized waveforms for a 2D fluid/fluid model. The cyan, magenta, and yellow lines indicate coupled-domain MFD (CPLD), SEM (SPECFEM2D), and single-domain (WELDED) solutions, respectively: wavefield components (a) $\bar{v}_z$ at x = 128 m, (b) $\bar{v}_x$ at x = 128 m, (c) $\bar{v}_z$ at x = 928 m, (d) $\bar{v}_x$ at x = 928 m, (e) $\bar{v}_z$ at x = 1328 m, and (f) $\bar{v}_x$ at x = 1328 m. The depth $z = 804$ m is the same for all traces.

$\bar{v}_z$- and $\bar{v}_x$-components is dominated by the surface wave (Figure 12), which is further confirmed by Figure 13. Hence, the late arrival in our previous experiment (Figure 11) was formed by the surface wave which was strongly distorted in the welded solution.

2D fluid/solid VTI interface

Next, we make the solid transversely isotropic with a vertical symmetry axis (VTI). The dimensions and other modeling parameters are kept the same. The anisotropy in the solid influences the amplitudes and phases of the solutions obtained by the coupled-domain and welded methods (Figure 14). For a quantitative comparison, we again analyze traces at three locations marked by the red lines at x = 680, 1400, and 1800 m (at $z = 84$ m). As before, the coupled-domain (cyan) and SEM (magenta) solutions are close to one another (Figure 15).

As previously, we apply absorbing boundary conditions on all four sides of the model and observe two interference arrivals (PP and PS) and the surface Stoneley (Scholte) wave (Figure 16). The dominant event on the $\bar{v}_z$- and $\bar{v}_x$-components (Figure 17) is again the late-arriving surface wave. Likewise, the slowest event in our previous test (Figure 15) was formed by the surface wave that interfered with the free-surface arrivals. The PP and PS modes, clearly visible in Figure 17, also interfered with free-surface reflections in our previous experiment (Figure 15). The welded solution distorts the amplitudes and phases of all arrivals because of the incorrect boundary conditions at the fluid/solid interface. Note that the relative amplitude of the surface wave, as expected, increases with offset (Figure 15b and 15f).

Finally, the algorithm is tested on a strongly heterogeneous VTI Marmousi model (Bourgeois et al., 1991) with the Thomsen parameters (see Tsvankin, 2012) shown in Figure 18. We inject a Ricker-wavelet source with the 25 Hz peak frequency at [x,z] = [2405,560] m. Figure 19 displays wavefield snapshots for the coupled-domain and welded solutions. There are slight phase

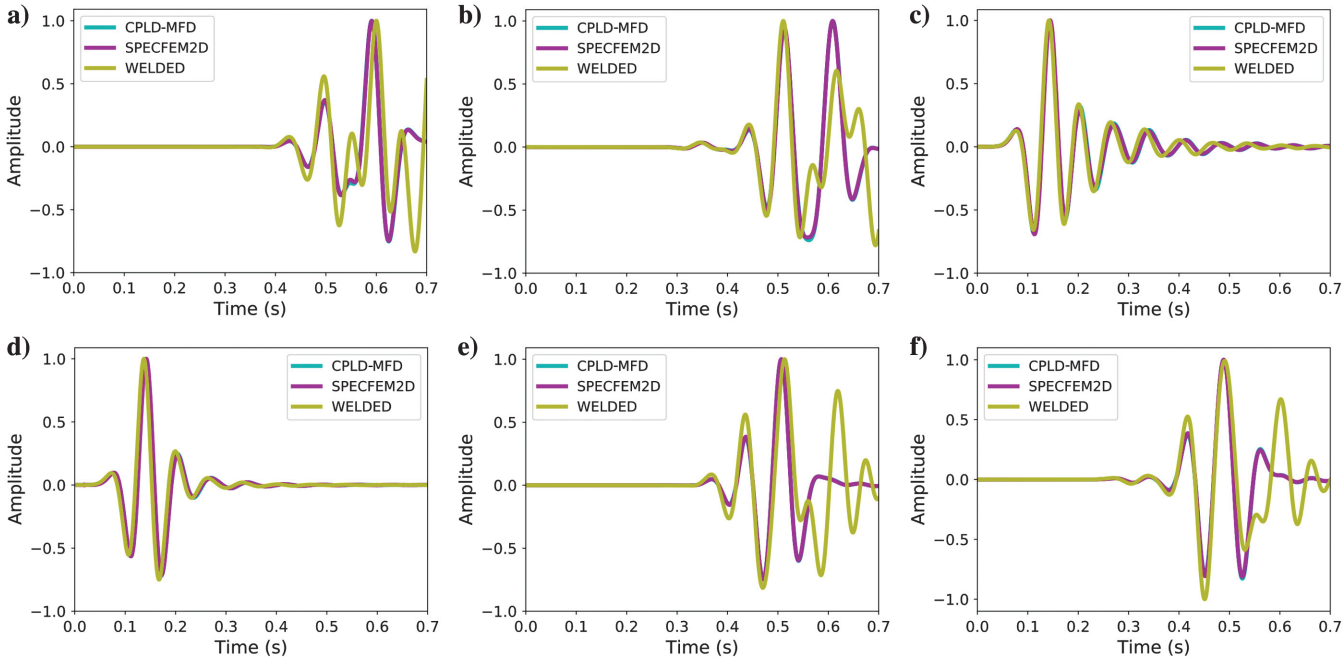

Figure 11. Normalized waveforms for the model from Figure 10. The cyan, magenta and yellow lines mark the coupled-domain MFD (CPLD), SEM (SPECFEM2D), and single-domain (WELDED) solutions, respectively. The components (a) $\bar{v}_z$ at x = 608 m, (b) $\bar{v}_x$ at x = 608 m, (c) $\bar{v}_z$ at x = 1250 m, (d) $\bar{v}_x$ at x = 1250 m, (e) $\bar{v}_z$ at x = 1688 m, and (f) $\bar{v}_x$ at x = 1688 m.

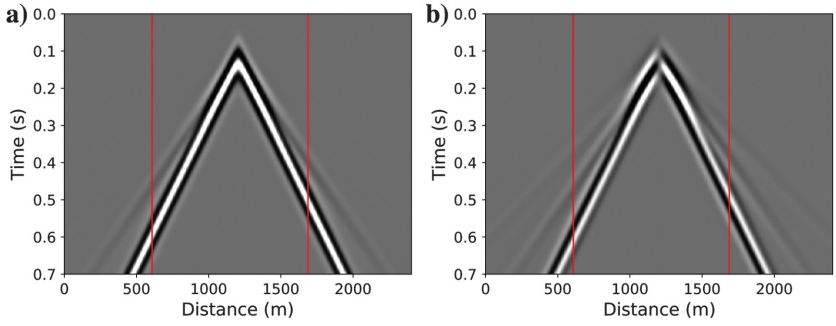

Figure 12. Shot gathers of the (a) $\bar{v}_z$- and (b) $\bar{v}_x$-components computed by the coupled-domain method for the model from Figure 10 with CPML boundary conditions applied on all four sides. The solid is isotropic with P-wave velocity $V_P = 2500$ m/s, S-wave velocity $V_S = 1600$ m/s, and density $\rho^s = 2000$ kg/m^3. The fluid has velocity $c^f = 1500$ m/s and density $\rho^f = 1000$ kg/m^3.

and amplitude differences in the areas above and below the interface and some differences in amplitudes throughout the model. In addition to the shot gathers computed with the coupled-domain (Figure 20a and 20b) and welded (Figure 20c and 20d) techniques, we extract traces for the receivers located at x = 1500, 2500, and x = 3500 m ($z = 610$ m). There are significant differences between the traces for the $\bar{v}_z$- and $\bar{v}_x$-components generated by the two techniques (Figure 21). The combination of the incorrect boundary conditions with the heterogeneity and anisotropy in the solid leads to complicated distortions in the results of the welded wavefield modeling. Clearly, it is extremely important to incorporate the correct boundary conditions for models involving a fluid/solid interface.

DISCUSSION

Our MFD methodology uses an FSG approach which is more computationally expensive than the conventional staggered grids. The memory requirements and computational cost for our algorithm are approximately two times for 2D and four times for 3D those of SSGs. But our technique yields better grid-dispersion properties because the solution of the same order can be obtained by using fewer points per wavelength compared with SSG.

An important advantage of the developed MFD methodology for handling fluid/solid interfaces is the reduction in memory requirements and computational cost for large-scale modeling,

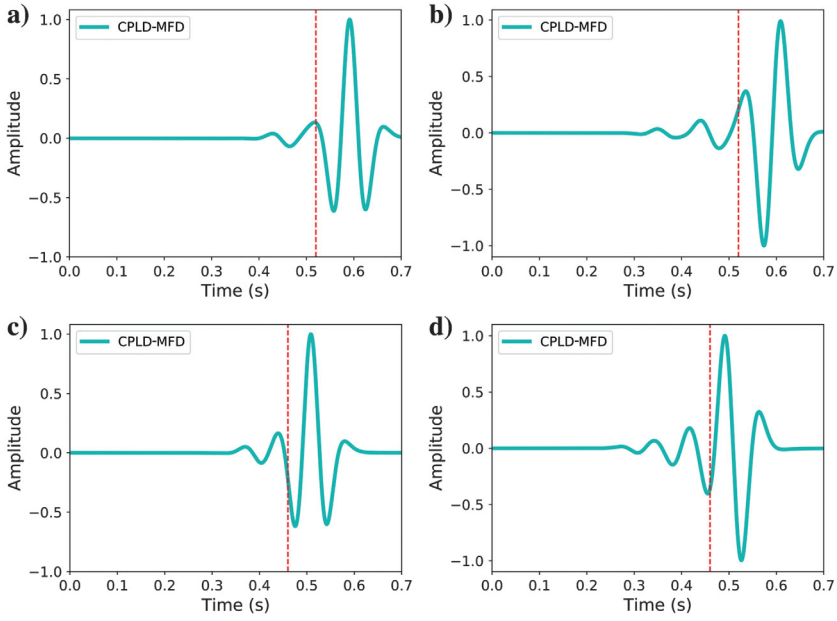

Figure 13. Normalized waveforms computed by the coupled-domain method for the 2D fluid/solid model from Figure 10. The vertical red line marks the surface-wave arrival: the components (a) $\bar{v}_z$ at x = 608 m, (b) $\bar{v}_x$ at x = 608 m, (c) $\bar{v}_z$ at x = 1688 m, and (d) $\bar{v}_x$ at x = 1688 m.

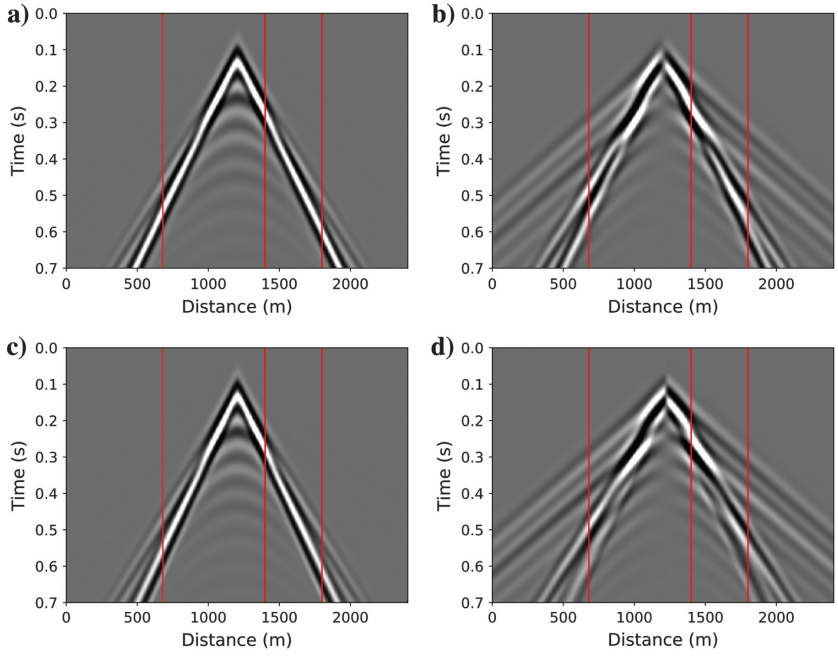

Figure 14. Shot gathers for a 2D model that includes a fluid overlaying a VTI solid. The Thomsen (1986; see also Tsvankin, 2012) parameters for the solid are the P-wave vertical velocity $V_{P0} = 2500$ m/s, the S-wave vertical velocity $V_{S0} = 1600$ m/s, $\epsilon = 0.2$, $\delta = 0.1$, and $\rho^s = 2000$ kg/m^3. The fluid has the velocity $c^f = 1500$ m/s and density $\rho^f = 1000$ kg/m^3. The coupled-domain solutions for the (a) $\bar{v}_z$- and (b) $\bar{v}_x$-components. The welded-domain solutions for the (c) $\bar{v}_z$- and (d) $\bar{v}_x$-components.

DOI:10.1190/geo2020-0092.1

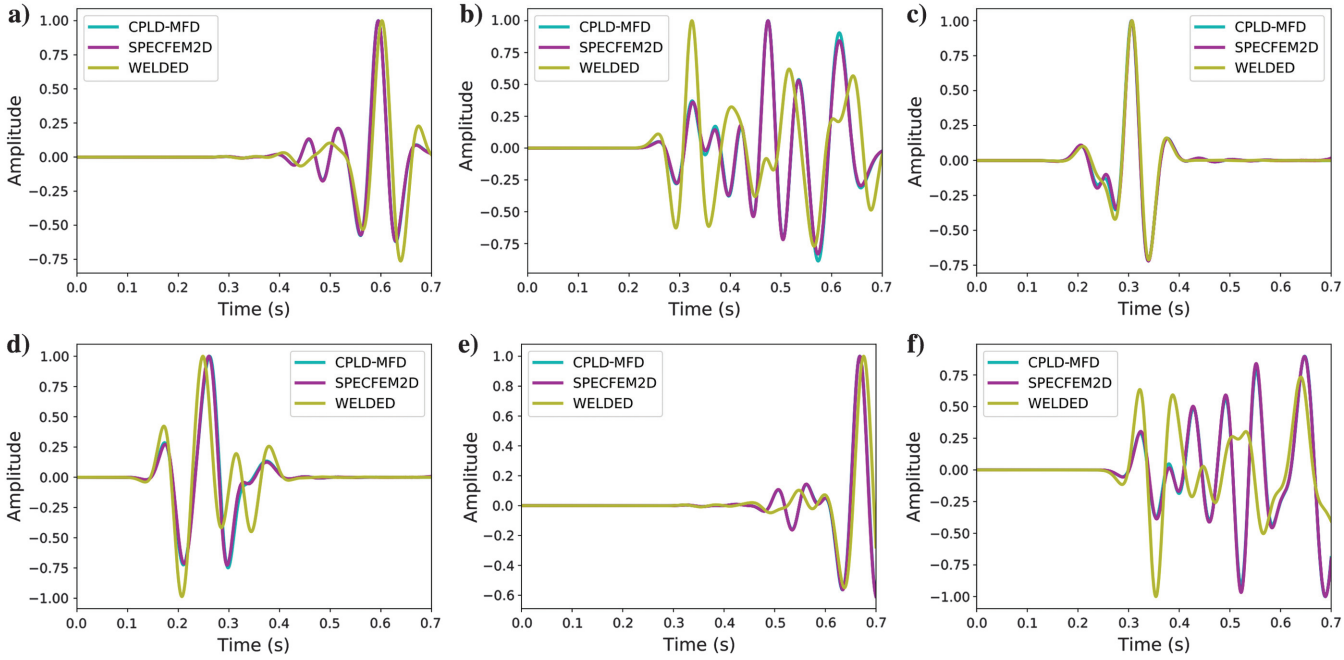

Figure 15. Normalized traces for the model from Figure 14. Cyan, magenta, and yellow lines mark the coupled-domain MFD (CPLD), SEM (SPECFEM2D), and single-domain (WELDED) solutions, respectively. The components (a) $\bar{v}_z$ at $x = 680$ m, (b) $\bar{v}_x$ at $x = 680$ m, (c) $\bar{v}_z$ at $x = 1400$ m, (d) $\bar{v}_x$ at $x = 1400$ m, (e) $\bar{v}_z$ at $x = 1800$ m, and (f) $\bar{v}_x$ at $x = 1800$ m.

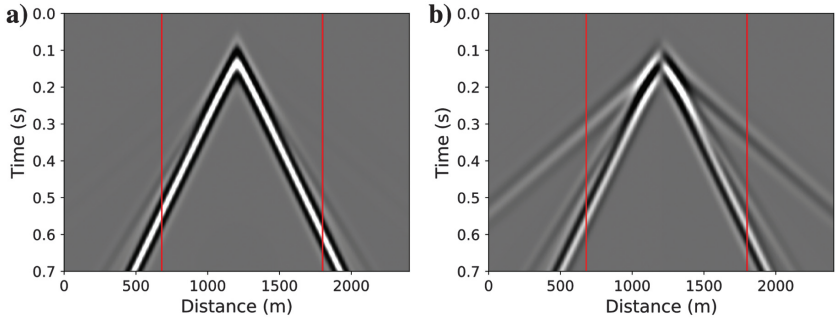

Figure 16. Shot gathers of the (a) $\bar{v}_z$- and (b) $\bar{v}_x$-components computed by the coupled-domain method for the model from Figure 14.

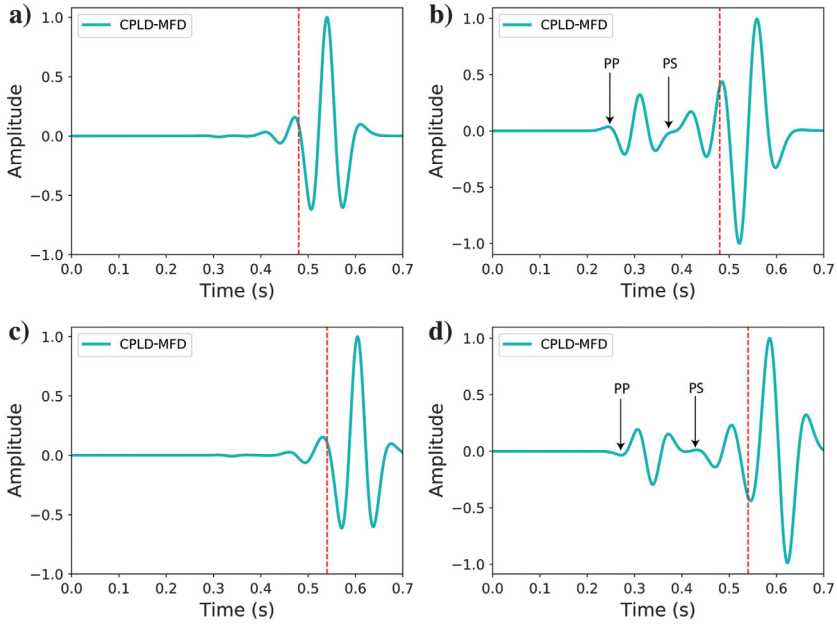

Figure 17. Normalized traces for the wavefield from Figure 16. The vertical red line marks the surface-wave arrival. The arrows mark the PP (formed by the head and transmitted PP-waves) and PS (formed by the head and transmitted PS-waves) interference arrivals. The components (a) $\bar{v}_z$ at $x = 680$ m, (b) $\bar{v}_x$ at $x = 680$ m, (c) $\bar{v}_z$ at $x = 1800$ m, and (d) $\bar{v}_x$ at $x = 1800$ m.

imaging, and inversion applications. Generally, the cost of solving the 3D elastic anisotropic wave equation (in terms of the memory and computational time) is roughly eight times that for the acoustic wave equation. In marine seismic applications, if 25% of the model consists of a water layer, using a 3D acoustic wave propagator instead of its elastic anisotropic counterpart would save roughly 28% (25% in 2D) in memory storage and computational cost.

The approach presented in this paper can be extended to irregular sea-bottom bathymetry using vertically deformed meshes (Shragge, 2017). FSGs make it possible to handle models with complex bathymetry and realistic anisotropic symmetry (e.g., tilted transversely isotropic or tilted orthorhombic media). With such more advanced modeling algorithms, one can potentially extract additional information from multicomponent data recorded in ocean-bottom surveys, which should be highly beneficial for elastic anisotropic imaging and inversion.

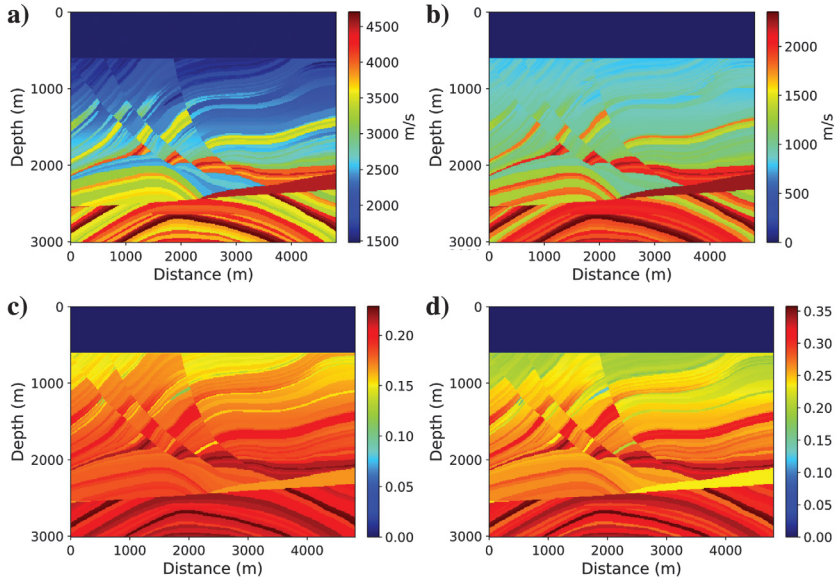

Figure 18. VTI Marmousi model with a 600-m thick water layer on top. The parameters (a) V_{P0}, (b) V_{S0}, (c) δ, and (d) ε.

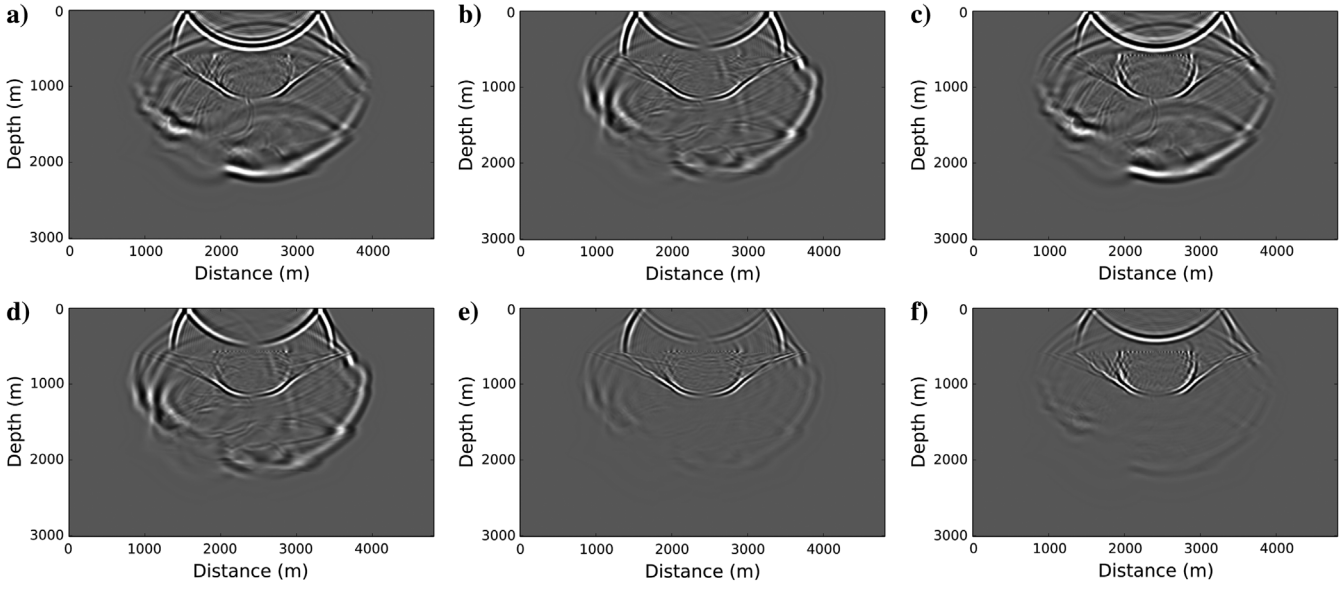

Figure 19. Representative wavefield snapshots for the CPLD (top row) and welded (middle row) solutions and the differences between them (bottom row). The components (a) $\bar{v}_z$ and (b) $\bar{v}_x$ generated by CPLD. The components (c) $\bar{v}_z$ and (d) $\bar{v}_x$ generated by the welded solution. The differences between (e) $\bar{v}_z$ and (f) $\bar{v}_x$ from the two methods.

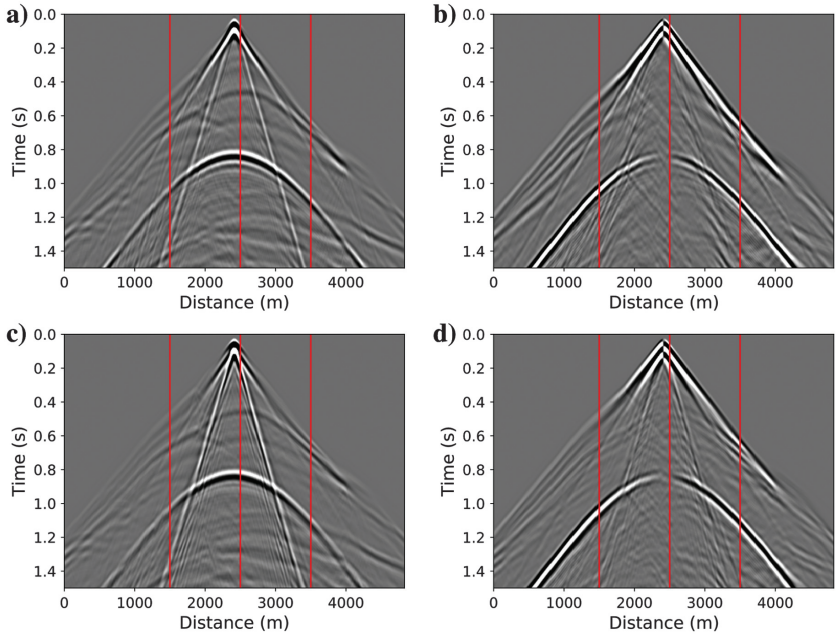

Figure 20. Shot gathers for the VTI Marmousi model (Figure 18). The coupled-domain solutions for the (a) $\bar{v}_z$- and (b) $\bar{v}_x$-components. The welded-domain solutions for the (c) $\bar{v}_z$- and (d) $\bar{v}_x$-components.

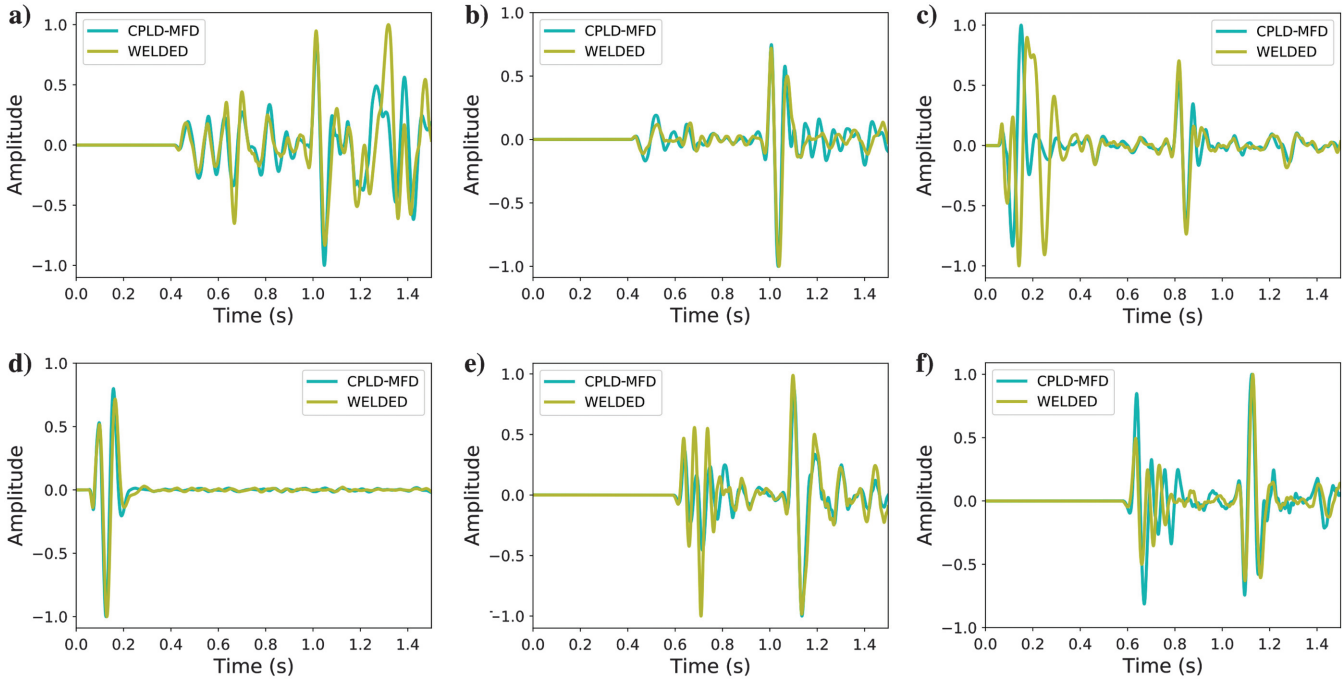

Figure 21. Normalized traces for the VTI Marmousi model (Figure 18). The cyan and yellow lines mark the coupled-domain MFD (CPLD) and single-domain (WELDED) solutions, respectively. The components (a) $\bar{v}_z$ at $x = 1500$ m, (b) $\bar{v}_x$ at $x = 1500$ m, (c) $\bar{v}_z$ at $x = 2500$ m, (d) $\bar{v}_x$ at $x = 2500$ m, (e) $\bar{v}_z$ at $x = 3500$ m, and (f) $\bar{v}_x$ at $x = 3500$ m.

CONCLUSIONS

We presented an efficient MFD methodology implemented on FSGs for solving the coupled fluid/solid modeling problem where the solid medium can be generally anisotropic. The developed uniform wavefield solution is spatially accurate to the fourth order both at the interface and in the model interior. The interface is handled using a split-node technique, and the boundary conditions are satisfied by using averaging for one set of the grids. The mimetic points on the other set of the grids are updated using the continuity of the spatial wavefield derivatives obtained from the acoustic and elastic wave equations.

Our proposed MFD methodology is validated by comparing the results with those obtained by the spectral-element method. Comparison with so-called "welded" solutions, which treat the fluid

medium as a solid, demonstrates that the amplitude and phase of the surface waves modeled with such welded solvers are substantially distorted. Therefore, it is essential to implement the correct boundary conditions at the fluid/solid interface in FD algorithms. Our modeling approach should have a substantial impact on the accuracy of elastic imaging and inversion.

ACKNOWLEDGMENTS

We thank the sponsors of the Center for Wave Phenomena (CWP) at Colorado School of Mines for their support. We are grateful to T. Konuk (CWP) and J. de la Puente (Barcelona Supercomputing Center) for many useful discussions. Spectral-element solutions were computed using code SPECFEM2D (https://geodynamics.org/cig/software/specfem2d/).

DATA AND MATERIALS AVAILABILITY

Data associated with this research are confidential and cannot be released.

APPENDIX A

MFD OPERATORS

The 1D mimetic divergence operator $\mathbf{D} \in \mathbb{R}^{(N+2,N+1)}$ (Corbino and Castillo, 2017) operating on the N-point grid is given by

$$\mathbf{D}_i = \frac{1}{h}\begin{bmatrix} 0 & 0 & 0 & 0 & 0 & 0 & \dots & \dots & \dots \\ \frac{-11}{12} & \frac{17}{24} & \frac{3}{8} & \frac{-5}{24} & \frac{1}{24} & 0 & \dots & \dots & \dots \\ 0 & \frac{1}{24} & \frac{-9}{8} & \frac{9}{8} & \frac{-1}{24} & 0 & \dots & \dots & \dots \\ 0 & 0 & \frac{1}{24} & \frac{-9}{8} & \frac{9}{8} & \frac{-1}{24} & 0 & \dots & \dots \\ \vdots & \vdots & \vdots & \ddots & \ddots & \ddots & \vdots & \vdots & \vdots \\ \dots & \dots & 0 & \frac{1}{24} & \frac{-9}{8} & \frac{9}{8} & \frac{-1}{24} & 0 & \dots \\ \dots & \dots & \dots & 0 & \frac{-1}{24} & \frac{5}{24} & \frac{-3}{8} & \frac{-17}{24} & \frac{11}{12} \\ \dots & \dots & \dots & 0 & 0 & 0 & 0 & 0 & 0 \end{bmatrix}, \tag{A-1}$$

where the dots indicate the repetition of the stencil coefficients in the corresponding direction, and h is the spatial discretization along the ith direction. The 1D mimetic gradient operator $\mathbf{G} \in \mathbb{R}^{(N+1,N+2)}$ (Corbino and Castillo, 2017) for the N-point grid can be written as

$$\mathbf{G}_i = \frac{1}{h}\begin{bmatrix} \frac{-352}{105} & \frac{35}{8} & \frac{-35}{24} & \frac{21}{40} & \frac{-5}{56} & 0 & \dots & \dots & \dots \\ \frac{16}{105} & \frac{-31}{24} & \frac{29}{24} & \frac{-3}{40} & \frac{1}{168} & 0 & \dots & \dots & \dots \\ 0 & \frac{1}{24} & \frac{-9}{8} & \frac{9}{8} & \frac{-1}{24} & 0 & \dots & \dots & \dots \\ \vdots & \vdots & \vdots & \ddots & \ddots & \ddots & \vdots & \vdots & \vdots \\ \dots & \dots & 0 & \frac{1}{24} & \frac{-9}{8} & \frac{9}{8} & \frac{-1}{24} & 0 & \dots \\ \dots & \dots & \dots & 0 & \frac{-1}{168} & \frac{3}{40} & \frac{-29}{24} & \frac{31}{24} & \frac{-16}{105} \\ \dots & \dots & \dots & 0 & \frac{5}{56} & \frac{-21}{40} & \frac{35}{24} & \frac{-35}{8} & \frac{352}{105} \end{bmatrix}. \tag{A-2}$$

REFERENCES

Bourgeois, A., M. Bourget, P. Lailly, M. Poulet, P. Ricarte, R. Versteeg, and G. Grau, 1991, Marmousi, model and data, *in* R. Versteeg and G. Grau, eds., The Marmousi Experience, Proceedings of the 1990 EAEG Workshop on Practical Aspects of Seismic Data Inversion: EAGE, 5–16.

Castillo, J. E., and R. Grone, 2003, A matrix analysis approach to higher-order approximations for divergence and gradients satisfying a global conservation law: SIAM Journal on Matrix Analysis and Applications, **25**, 128–142, doi: 10.1137/S0895479801398025.

Castillo, J. E., and G. F. Miranda, 2013, Mimetic discretization methods: Chapman and Hall/CRC.

Corbino, J., and J. Castillo, 2017, Computational science & engineering: San Diego State University.

De Basabe, J. D., and M. K. Sen, 2014, A comparison of finite-difference and spectral-element methods for elastic wave propagation in media with a fluid-solid interface: Geophysical Journal International, **200**, 278–298, doi: 10.1093/gji/ggu389.

de Hoop, A. T., and J. H. Van der Hijden, 1984, Generation of acoustic waves by an impulsive point source in a fluid/solid configuration with a plane boundary: The Journal of the Acoustical Society of America, **75**, 1709–1715, doi: 10.1121/1.390970.

de la Puente, J., M. Ferrer, M. Hanzich, J. E. Castillo, and J. M. Cela, 2014, Mimetic seismic wave modeling including topography on deformed staggered grids: Geophysics, **79**, no. 3, T125–T141, doi: 10.1190/geo2013-0371.1.

Farfour, M., and W. J. Yoon, 2016, A review on multicomponent seismology: A potential seismic application for reservoir characterization: Journal of Advanced Research, **7**, 515–524, doi: 10.1016/j.jare.2015.11.004.

Hung, S.-H., and D. W. Forsyth, 1998, Modelling anisotropic wave propagation in oceanic inhomogeneous structures using the parallel multidomain pseudo-spectral method: Geophysical Journal International, **133**, 726–740, doi: 10.1046/j.1365-246X.1998.00526.x.

Käser, M., and M. Dumbser, 2008, A highly accurate discontinuous Galerkin method for complex interfaces between solids and moving fluids: Geophysics, **73**, no. 3, T23–T35, doi: 10.1190/1.2870081.

Komatitsch, D., C. Barnes, and J. Tromp, 2000, Wave propagation near a fluid-solid interface: A spectral-element approach: Geophysics, **65**, 623–631, doi: 10.1190/1.1444758.

Komatitsch, D., and R. Martin, 2007, An unsplit convolutional perfectly matched layer improved at grazing incidence for the seismic wave equation: Geophysics, **72**, no. 5, SM155–SM167, doi: 10.1190/1.2757586.

Konuk, T., and J. Shragge, 2020, Modeling full-wavefield time-varying sea-surface effects on seismic data: A mimetic finite-difference approach: Geophysics, **85**, no. 2, T45–T55, doi: 10.1190/geo2019-0181.1.

Kugler, S., T. Bohlen, T. Forbriger, S. Bussat, and G. Klein, 2007, Scholte-wave tomography for shallow-water marine sediments: Geophysical Journal International, **168**, 551–570, doi: 10.1111/j.1365-246X.2006.03233.x.

Lebedev, V. I., 1964, Difference analogues of orthogonal decompositions, basic differential operators and some boundary problems of mathematical physics. I: USSR Computational Mathematics and Mathematical Physics, **4**, 69–92, doi: 10.1016/0041-5553(64)90240-X.

Levander, A. R., 1988, Fourth-order finite-difference P-SV seismograms: Geophysics, **53**, 1425–1436, doi: 10.1190/1.1442422.

Lisitsa, V., and D. Vishnevskiy, 2010, Lebedev scheme for the numerical simulation of wave propagation in 3D anisotropic elasticity: Geophysical Prospecting, **58**, 619–635, doi: 10.1111/j.1365-2478.2009.00862.x.

Muir, F., J. Dellinger, J. Etgen, and D. Nichols, 1992, Modeling elastic fields across irregular boundaries: Geophysics, **57**, 1189–1193, doi: 10.1190/1.1443332.

Padilla, F., M. de Billy, and G. Quentin, 1999, Theoretical and experimental studies of surface waves on solid–fluid interfaces when the value of the fluid sound velocity is located between the shear and the longitudinal ones in the solid: The Journal of the Acoustical Society of America, **106**, 666–673, doi: 10.1121/1.427084.

Petersson, N. A., and B. Sjögreen, 2015, Wave propagation in anisotropic elastic materials and curvilinear coordinates using a summation-by-parts finite difference method: Journal of Computational Physics, **299**, 820–841, doi: 10.1016/j.jcp.2015.07.023.

Qu, Y., Z. Guan, J. Li, and Z. Li, 2020, Fluid-solid coupled full-waveform inversion in the curvilinear coordinates for ocean-bottom cable data: Geophysics, **85**, no. 3, R113–R133, doi: 10.1190/geo2018-0743.1.

Robertsson, J. O., and A. Levander, 1995, A numerical study of seafloor scattering: The Journal of the Acoustical Society of America, **97**, 3532–3546, doi: 10.1121/1.412439.

Rojas, O., 2007, Mimetic finite difference modeling of 2D elastic P-SV wave propagation: Qualifying examination report, Computational Science Research Center, San Diego State University.

Rojas, O., S. Day, J. Castillo, and L. A. Dalguer, 2008, Modelling of rupture propagation using high-order mimetic finite differences: Geophysical Journal International, **172**, 631–650, doi: 10.1111/j.1365-246X.2007.03651.x.

Shragge, J., 2014, Solving the 3D acoustic wave equation on generalized structured meshes: A finite-difference time-domain approach: Geophysics, **79**, no. 6, T363–T378, doi: 10.1190/geo2014-0172.1.

Shragge, J., 2017, Tensorial elastodynamics for isotropic media on vertically deformed meshes: 87th Annual International Meeting, SEG, Expanded Abstracts, 4034–4038, doi: 10.1190/segam2017-17779399.1.
Shragge, J., and B. Tapley, 2017, Solving the tensorial 3D acoustic wave equation: A mimetic finite-difference time-domain approach: Geophysics, **82**, no. 4, T183–T196, doi: 10.1190/geo2016-0691.1.
Stephen, R., 1983, A comparison of finite difference and reflectivity seismograms for marine models: Geophysical Journal International, **72**, 39–57, doi: 10.1111/j.1365-246X.1983.tb02803.x.
Sun, Y.-C., W. Zhang, J.-K. Xu, and X. Chen, 2017, Numerical simulation of 2-D seismic wave propagation in the presence of a topographic fluid–solid interface at the sea bottom by the curvilinear grid finite-difference method: Geophysical Journal International, **210**, 1721–1738, doi: 10.1093/gji/ggx257.
Thomsen, L., 1986, Weak elastic anisotropy: Geophysics, **51**, 1954–1966, doi: 10.1190/1.1442051.
Tomar, G., N. M. Shapiro, A. Mordret, S. C. Singh, and J.-P. Montagner, 2016, Radial anisotropy in Valhall: Ambient noise-based studies of Scholte and Love waves: Geophysical Journal International, **208**, 1524–1539, doi: 10.1093/gji/ggw480.
Tsvankin, I., 2012, Seismic signatures and analysis of reflection data in anisotropic media, 3rd ed.: Society of Exploration Geophysicists.
Virieux, J., 1986, P-SV wave propagation in heterogeneous media: Velocity-stress finite-difference method: Geophysics, **51**, 889–901, doi: 10.1190/1.1442147.
Voinovich, P., A. Merlen, E. Timofeev, and K. Takayama, 2003, A Godunov-type finite-volume scheme for unified solid-liquid elastodynamics on arbitrary two-dimensional grids: Shock Waves, **13**, 221–230, doi: 10.1007/s00193-003-0211-4.
Zhang, W., Z. Zhang, and X. Chen, 2012, Three-dimensional elastic wave numerical modelling in the presence of surface topography by a collocated-grid finite-difference method on curvilinear grids: Geophysical Journal International, **190**, 358–378, doi: 10.1111/j.1365-246X.2012.05472.x.

Biographies and photographs of the authors are not available.